

PROCEEDINGS OF SPIE

[SPIDigitalLibrary.org/conference-proceedings-of-spie](https://www.spiedigitallibrary.org/conference-proceedings-of-spie)

Characterization of AlMn TES impedance, noise, and optical efficiency in the first 150 mm multichroic array for Advanced ACTPol

Crowley, Kevin, Choi, Steve, Kuan, Jeffrey, Austermann, Jason, Beall, James, et al.

Kevin T. Crowley, Steve K. Choi, Jeffrey Kuan, Jason A. Austermann, James A. Beall, Rahul Datta, Shannon M. Duff, Patricio A. Gallardo, Matthew Hasselfield, Shawn W. Henderson, Shuay-Pwu P. Ho, Brian J. Koopman, Michael D. Niemack, Maria Salatino, Sara M. Simon, Suzanne T. Staggs, Edward J. Wollack, "Characterization of AlMn TES impedance, noise, and optical efficiency in the first 150 mm multichroic array for Advanced ACTPol," Proc. SPIE 9914, Millimeter, Submillimeter, and Far-Infrared Detectors and Instrumentation for Astronomy VIII, 991431 (16 September 2016); doi: 10.1117/12.2231999

SPIE.

Event: SPIE Astronomical Telescopes + Instrumentation, 2016, Edinburgh, United Kingdom

Characterization of AlMn TES Impedance, Noise, and Optical Efficiency in the First 150 mm Multichroic Array for Advanced ACTPol

Kevin T. Crowley^a, Steve K. Choi^a, Jeffrey Kuan^a, Jason E. Austermann^b, James A. Beall^b, Rahul Datta^c, Shannon M. Duff^b, Patricio A. Gallardo^e, Matthew Hasselfield^d, Shawn W. Henderson^e, Shuay-Pwu P. Ho^a, Brian J. Koopman^e, Michael D. Niemack^e, Maria Salatino^a, Sara M. Simon^c, Suzanne T. Staggs^a, and Edward J. Wollack^f

^aJoseph Henry Laboratories of Physics, Jadwin Hall, Princeton University, Princeton, NJ, USA 08544

^bNIST Quantum Devices Group, 325 Broadway Mailcode 817.03, Boulder, CO, USA 80305

^cDepartment of Physics, University of Michigan, Ann Arbor, MI, USA 48103

^dDepartment of Astronomy and Astrophysics, The Pennsylvania State University, University Park, PA, USA 16802

^eDepartment of Physics, Cornell University, Ithaca, NY, USA 14853

^fGoddard Space Flight Center, Greenbelt, MD, 20771, USA

ABSTRACT

The Advanced ACTPol (AdvACT) upgrade to the Atacama Cosmology Telescope features large arrays of multichroic pixels consisting of two orthogonal-polarization pairs of superconducting bolometers at two observing frequency bands. We present measurements of the detector properties and noise data in a subset of a fielded multichroic array of AlMn transition-edge sensor (TES) detectors. In this array, the distribution of critical temperature T_c across detectors appears uniform at the percent level. The measured noise-equivalent power (NEP) distributions over ~ 1200 detectors are consistent with expectations. We find median NEPs of 4.0×10^{-17} W/ $\sqrt{\text{Hz}}$ for low-band detectors and 6.2×10^{-17} W/ $\sqrt{\text{Hz}}$ for high-band detectors under covered-window telescope test conditions with optical loading comparable to observing with precipitable water vapor ~ 0.5 mm. Lastly, we show the estimated detector optical efficiency, and demonstrate the ability to perform optical characterization over hundreds of detectors at once using a cryogenic blackbody source.

Keywords: Transition edge sensors, bolometers, CMB, electrothermal model

1. INTRODUCTION

Advanced ACTPol is a staged upgrade of the receiver at the focus of the Atacama Cosmology Telescope (ACT) at a high-altitude site in Chile. Sky polarization will be measured in bands with five central frequencies (28, 41, 90, 150, 230 GHz) in wide regions of the southern sky¹ through cold reimaging optics and an ambient-temperature, rapidly-rotating half-wave plate. The AdvACT focal plane will consist of new multichroic arrays with four manganese-doped aluminum TES bolometers per pixel, a polarization pair at each of two frequencies. Optical signals couple to these detectors through a silicon platelet feedhorn array² feeding a planar orthomode transducer (OMT). The OMT signals pass through microstrip diplexers and stub filters on pixel before being combined and terminated in a lossy gold meander, which heats the TESes.³

This measurement chain rests upon the TES detectors which convert optical power into measurable current. Initial tests of these devices began with verification of the ability to reliably tune TES device parameters, such

Further author information: (Send correspondence to K.T.C., S.K.C.)

K.T.C.: E-mail: ktc2@princeton.edu

S.K.C.: E-mail: khc@princeton.edu

as T_c , through a combined doping and heat treatment process.⁴ The first AdvACT high-frequency (HF) array was fabricated on a single 150 mm wafer.⁵ Early results indicate the 150 mm development effort led to good uniformity in the detector thermal properties, such as 1-2% variation in T_c over the array.

In this work, the AlMn devices are investigated to determine whether their electrothermal properties can be well-explained by a simple bolometer model⁶ – a thermal weak link coupling a single lumped-element heat capacity to the thermal bath. Results for initial impedance and noise measurements are presented, along with details on the impedance data analysis and generation of the noise model from extracted device parameters. Similar data gathered for the MoCu bilayers of the ACTPol multichroic array³ are briefly discussed. For the AlMn sensors, a final electrothermal analysis, including gathering data during early-phase tests of the new array at the ACT site, is underway.

In addition to these dark tests, the optical coupling of the AlMn devices through the silicon feedhorn array is probed by illuminating the array with a cryogenic blackbody source in laboratory. Changes in the cold load temperature between ~ 11 K and ~ 22 K lead to measurable changes in the bias power to which we compare the expected optical power and estimate the optical efficiency. We demonstrate the ability to perform this optical characterization in laboratory on hundreds of detectors over the 150 mm wafer.

In short, this paper presents work in progress towards a full understanding of detector electrothermal behaviors and optical response for the purpose of characterizing these devices in preparation for future science analysis. These measurements will improve our understanding of how intrinsic detector sensitivities, i.e. NEPs, translate to instantaneous array sensitivity and, eventually, noise level in the AdvACT CMB maps.

In Section 2, we describe important array characteristics and provide brief descriptions of the testing configurations in the laboratory and on the telescope. Section 3 discusses measurements and results for detector testing of electrothermal model parameters and noise levels in both testbeds (laboratory and telescope). Section 4 specifically discusses laboratory measurements of optical efficiency. We conclude in Section 5.

2. EXPERIMENTAL SETUP

The integration of the first AdvACT array, the high-frequency array (known as HF, which operates at 150 and 230 GHz), is described in detail in Ref. 7 in these proceedings. This section briefly describes the elements of the system important for the tests described in Sections 3 and 4.

For the HF array, TESes are multiplexed using time-division switching and cryogenic chips fabricated at NIST.⁸ A separate set of chips, known as interface chips, provide shunt resistors on the TES bias line and series Nyquist inductors, the latter to prevent aliasing from high-frequency detector noise. We identify each detector by its column and row address in the multiplexing scheme.

In this version of time-division SQUID-multiplexed readout, each TES detector has its current coupled to a superconducting quantum interference device (SQUID). This first-stage SQUID is kept in a flux-locked loop by a separate feedback circuit with a coupling coil. A flux-activated switch controls which row is on at any time, while all columns of detectors are read out in parallel. Each column shares a SQUID series array amplifier through which the first-stage SQUID signal passes before being used to correct the error at the first-stage flux-locked loop. A warm Multi-channel Control Electronics (MCE) readout crate,⁹ designed and built by the team at UBC, manages all SQUID and detector biases, as well as the row switching parameters, feedback readout, and synchronization. A detailed overview of the multiplexing chip testing, processing, and integration for the HF array can be found in Ref. 10 in these proceedings.

The fully-integrated array is packaged in a gold-plated copper structure containing the detector wafer stack resting on the silicon platelet feedhorns and the array's FR4-laminate printed-circuit board (PCB), the latter supporting wiring chips affixed with rubber cement to the PCB and multiplexing chips and interface chips epoxied to the wiring chip.¹¹ In laboratory tests, the base-temperature stage is the mixing-chamber plate of an Oxford Instruments Triton 400 dilution refrigerator (DR). Despite the large mass to be cooled, we achieve an unheated base temperature of $\lesssim 40$ mK. For normal operation, a heater controlled by a PI feedback loop maintains array temperatures between 80 and 200 mK. A Lakeshore controller (AC370) runs the PI loop and makes a 4-lead AC-bridge measurement of the resistance of our RuOx sensors. The control temperature is measured at the

detector clamp ring supporting the detector wafer and feedhorns in these tests.¹¹ In the field, cooling is provided by a custom Janis DR whose mixing chamber connects to the array via a cold finger.¹² Temperature control is open-loop, with an achieved base temperature near 100mK while cooling the HF array and two already-present ACTPol arrays.

3. DARK MEASUREMENTS

In this section we discuss the collection of dark measurements performed on the first HF array, both in laboratory tests performed at Princeton and at the ACT site. For laboratory tests, roughly a third of active detectors were coupled to horns illuminated by a cryogenic blackbody source, and so were not studied using the tests described in this section. For tests on the telescope, reflective aluminum foil covers are placed over the warm window to minimize loading from the ambient temperature environment. The total optical loading due to all optical elements in the cryostat and the covers themselves is estimated as ~ 5 pW and ~ 10 pW for the 150 GHz and 230 GHz detectors, respectively (see Section 3.2).

Dark tests probe the behavior of the TESes under an assumed electrothermal model. This model is the simple voltage-biased TES model used for studying these detectors and described in detail in Ref. 6. Our discussion uses the nomenclature found in this reference. Physically motivated extensions, e.g. those found in Ref. 13, which take into account the presence of non-TES heat capacities, will be studied with future HF array datasets.

In order to study the TESes, the detectors are first voltage-biased through their superconducting transition, resulting in an I-V curve. These data allow the optimal bias for a group of detectors sharing a bias line to be found for a given target TES resistance, usually quoted as a fraction or percentage of R_N , the TES normal resistance. It is also the means by which the current and voltage at a given TES bias point (in $\%R_N$) are calculated.

Besides optimal biasing, we can study the behavior of I-V curves across a range of bath temperatures to acquire fundamental TES electrothermal parameters like critical temperature T_c and weak-link thermal conductance G . Saturation power P_{sat} is defined as the power at the TES at which the device's operating resistance equals 90% R_N . Assuming thermal energy balance for the TES island with no optical power present and a narrow TES transition in temperature, we define parameters κ and n by writing

$$P_{\text{sat}} = \kappa(T_c^n - T_{\text{bath}}^n). \quad (1)$$

We then define the effective thermal conductance G as

$$G \equiv \frac{dP_{\text{sat}}}{dT_c} = n\kappa T_c^{n-1}. \quad (2)$$

A three-parameter fit to P_{sat} vs. T_{bath} yields estimates for κ , n , and T_c . Detailed results on the uniformity of these parameters in the first HF array, which are crucial for uniform detector biasing under atmospheric optical loading, can be found in Ref. 14 in these proceedings. For this work, parameter values extracted from I-V data taken at multiple bath temperatures are used throughout the following sections to estimate electrothermal parameters and compare achieved noise to expectations. For the purposes of the dark tests reported here, we use laboratory results for the devices under study. In these results, we find 150 GHz detectors have average $\langle G \rangle = 370 \pm 20$ pW/K and average $\langle T_c \rangle = 164 \pm 3$ mK, where the spread indicates sample standard deviation of ~ 400 dark detectors. For 230 GHz detectors, $\langle G \rangle = 720 \pm 30$ pW/K and $\langle T_c \rangle = 165 \pm 3$ mK. The achieved T_c should be compared to the AdvACT target of 160 mK.

3.1 Impedance

To measure other parameters in the simple electrothermal model, a swept-sine measurement of device impedance is performed. In practice, measurement bandwidth is first increased beyond the usual ~ 400 Hz sampling frequency to the multiplexing rate of 7.8 kHz. An I-V curve taken just prior is analyzed for a single device to find the bias at which the device under study is closest to a given $\%R_N$. A sine wave with DC offset equal to this bias value and amplitude of 3 mV is then introduced to the bias line, and the output feedback signal is

measured. The input signal is not recorded by the MCE as it is being generated, but confirmation of the input's digital approximation to a sine wave can be obtained with a separate acquisition. We perform tests on both HF array AlMn devices and ACTPol MoCu devices.

A fit to the feedback signal for the device is performed, in which the measured frequency, amplitude, phase, and a linear baseline are free parameters. From the recovered amplitude and phase parameters, the voltage transfer function at a given frequency is calibrated into dimensionless units using MCE and bias-circuit constants, i.e. resistor values, mutual inductance ratios, etc. The complex transfer function is then stored while further analysis allows the Thevenin-equivalent TES bias circuit to be calibrated. This is done using voltage transfer functions acquired with the TES in its superconducting and normal states, following the work of Refs. 15 on thermistors and 16 on TES bolometers. From these two complex transfer functions and the measured normal resistance, the Thevenin-equivalent input voltage and series equivalent impedance Z_{eq} at each sine-wave frequency are estimated.

Since the equivalent circuit is known in the simplest case, we check the calibration using the expectation that $Z_{eq} \approx R_{sh} + i\omega L$, where R_{sh} is the shunt resistance in parallel with the device and L is the series inductance. Fig. 2 shows a fit of the imaginary part of Z_{eq} to a line, yielding L from the slope. A single R_{sh} value is estimated as the inverse variance-weighted average of the real parts of Z_{eq} at all frequencies. Previous four-lead measurements of the shunt resistors across a set of similar interface chips give an expected value of R_{sh} of $\sim 210 \mu\Omega$ averaged over 60 detector lines. Given reasonable spread within the sample, the fit value of $196 \pm 1 \mu\Omega$ is consistent with our expectation.

This measurement of Z_{eq} also allows us to compare measured and predicted noise with the TES superconducting and normal. Using the same set of parameters, laboratory noise data sampled at 7.8 kHz were compared to theoretical predictions assuming the presence of TES and shunt resistor Johnson noise, a one-pole L/R filter, and high-frequency SQUID noise aliased into the signal band by the sampling. Expected SQUID current noise

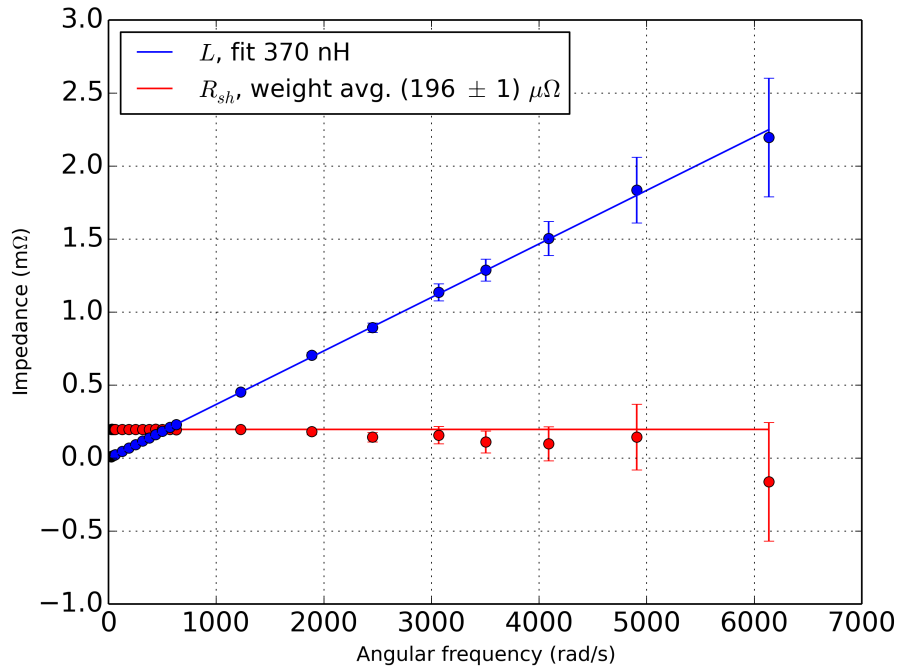


Figure 1: Calibration data for the equivalent impedance Z_{eq} in series with the TES. The legend shows the inverse variance-weighted average shunt resistance from the real part of Z_{eq} , and the inductance measured as the slope of the imaginary part of the impedance. The high-frequency (~ 400 Hz) falloff may be indicative of some parasitic impedance not captured by DC measurements of R_{sh} .

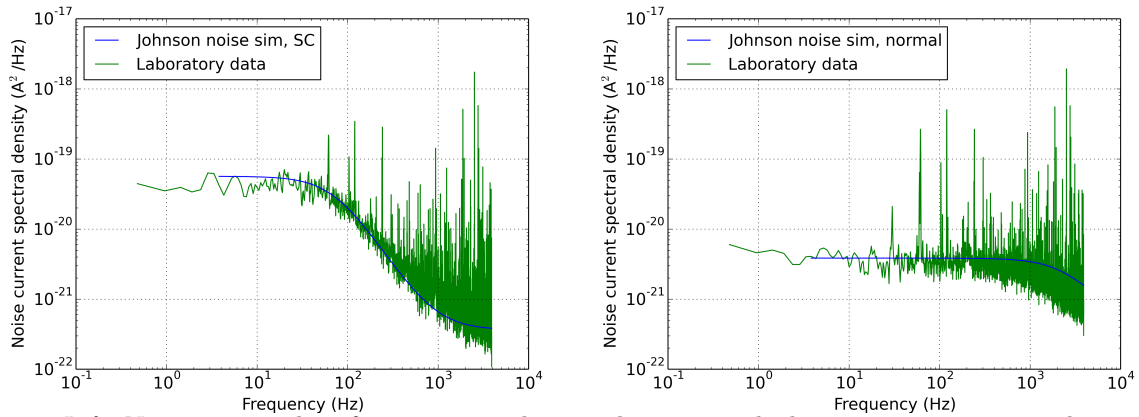


Figure 2: *Left*: Noise current data for a superconducting detector studied using swept-sine impedance measurements. The sample rate for these data is 7.8 kHz, the multiplexing frequency of the AdvACT HF array. All values in the simulation are derived from laboratory swept-sine data and measurements of SQUIDS similar to those in the TES readout circuit. *Right*: Noise current data for the same detector when acting as a normal resistor. We attribute lines in the spectra to pickup in our laboratory environment; there are more noticeable in the normal data due to the reduction in current noise with finite TES resistance.

is calculated based on values quoted in Ref. 8. Figure 1 shows the results of the comparison for the shunt and inductance values shown in Fig. 2. We note the sharp features (lines) in the frequency domain beginning at 60 Hz. However, we consider the model to be consistent with the data plus the electronic pickup.

A calibrated Z_{TES} dataset is shown in Fig. 3 for a detector at $50\%R_N$ and $T_{\text{bath}} \sim 100$ mK. This data set was taken on the telescope for a 150 GHz detector. We use calibrating normal and superconducting data from the dark laboratory tests.

In analyzing these data, we begin by fitting a semicircle to the data in the lower half of the complex plane. The coordinate of the circle's center and the circle radius are the free parameters. Next, the point at which the fit crosses the x -axis at high frequency is estimated as the x -coordinate of the center plus the radius. This point defines the dynamic resistance of the TES, $R_{\text{TES}}(1 + \beta)$, and from it the TES logarithmic current sensitivity β can be estimated. The estimated β and the radius are then combined to estimate the TES loop gain at this operating point, where the loop gain \mathcal{L} is defined as

$$\mathcal{L} = \frac{P_{\text{TES}}\alpha}{GT_c}, \quad (3)$$

where $\alpha = \frac{d \ln R}{d \ln T}$ of the TES resistance to temperature variations.

In Fig. 3, we observe a counter-clockwise trend of the data around the circle with increasing frequency, denoted by marker and error bar color. This confirms $\mathcal{L} > 1$, and under this assumption the loop gain is measured as $\mathcal{L} \sim 25$, corresponding to $\alpha \sim 160$. Such a large α is not unexpected for the AlMn devices. In contrast, for a 90 GHz MoCu detector on a separate array at $50\% R_N$ and same bath temperature, we measure $\alpha \sim 46$.

For the detector time constant, the trends with frequency of the real and imaginary parts of Z_{TES} are fitted separately. The more reliable fit is provided by the real part. The extracted effective time constant depends on the loop gain and the thermal time constant $\tau = C/G$, with C the effective heat capacity of the TES island. Extracting C from this measurement thus requires accurately estimating \mathcal{L} and τ probed by the swept sine. In the case of the MoCu detector whose α is mentioned above, $\mathcal{L} \sim 6.9$ and $\tau \sim 3.3$ ms. A consistency check on these results was performed by comparing the measured C of the MoCu detector to a separate estimate derived from square-wave input measurements, which probe the effective time constant for the TES response to optical signals.¹⁷ The impedance measurement gives an estimate of $C \sim 0.80$ pJ/K. An average across detectors comprising the same fabrication wafer in ACTPol's multichroic array gives $C = 0.84 \pm 0.12$ pJ/K.¹⁸

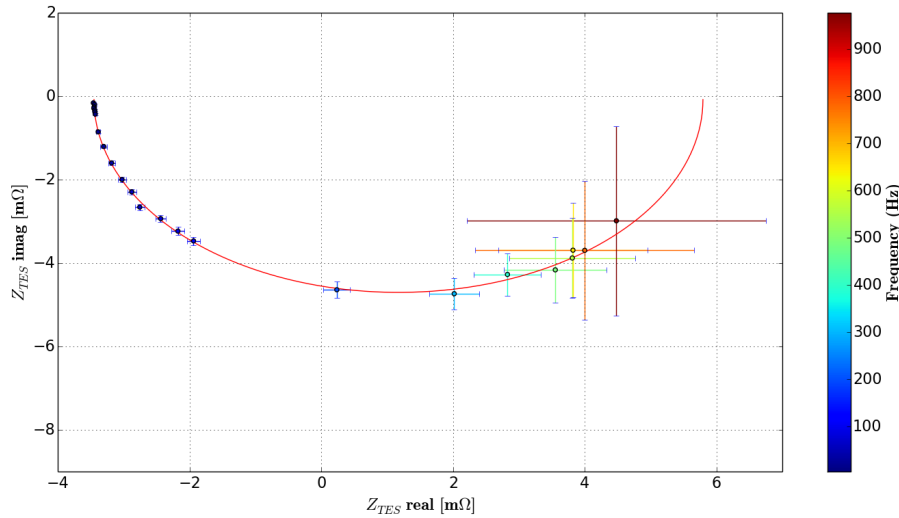


Figure 3: An example complex-impedance dataset for a 150 GHz AdvACT AlMn TES device acquired on the telescope. The counter-clockwise trend of the impedance with frequency confirms $\mathcal{L} > 1$. See text for more discussion.

In the case of AdvACT's HF array, the target heat capacity was chosen to ensure stable operation of the AlMn TES devices without sacrificing speed of device response. To achieve our target, the island heat capacity is tuned by altering the volume of a PdAu layer surrounding the TES.⁴ We measure a thermal time constant of $\tau \sim 16$ ms for the detector in Fig. 3. Measuring this thermal time constant in a distribution of detectors is needed.

As a final result, one can use the measured electrothermal parameters and calculate the expected effective time constant τ_{eff} , which is inversely related to \mathcal{L} and the $f_{3\text{dB}}$ of the low-pass filter response of the TES. For the HF array 150 GHz detector discussed here, this has been measured to be ~ 130 Hz at 50% R_N while trending inversely with the fraction of R_N at a given bias point. This behavior is expected, and is a result of changes to the device's current and temperature sensitivities, α and β .

3.2 Noise

In addition to the impedance data, high sample-rate noise data are taken during the same acquisition run as shown in Fig. 1. The detector is driven normal and rebased before taking this noise data. Under DC bias, we expect the signal in dark devices to be dominated by thermal link noise, defined as

$$\text{NEP}_{\text{TL}} = \sqrt{4k_B f_{\text{link}} G T_c^2} \text{ (W}/\sqrt{\text{Hz}}\text{)}. \quad (4)$$

The derivation of f_{link} as a non-equilibrium scaling factor can be found in Ref. 19. We expect for the silicon nitride legs that f_{link} should fall roughly in the interval $[0.5, 1]$. When f_{link} is used in this section, the value is estimated using the expression from Ref. 19 assuming thermal conductance through the legs scales as T^3 and that the TES temperature is T_c .

Figure 4 shows preliminary telescope noise data. At left is a measurement of NEP^2 , or power spectral density (PSD), vs. frequency for the detector studied in Fig. 3 under similar conditions. These data were taken directly after swept-sine measurements at 30%, 50%, and 70% of R_N with sample rate 7.8 kHz. The target bias for telescope observing runs will be 50% R_N . At this bias point, the noise data and model show good qualitative agreement. However, the preliminary datasets at 30% and 70% R_N have unexplained features still under investigation. We especially note the rise in noise level above ~ 100 Hz at 30% R_N as a particular target for study. With regard to the modeling of the noise spectra, the increased speed of the detector at 30% R_N made it difficult to constrain all parameters using the same set of sine frequencies as in the 50% and 70% R_N

data. The thin colored lines indicate the result of full electrothermal simulations of the detector noise power at each bias point as derived from parameter outputs of the swept-sine analysis. Like the simulation in Fig. 1, this includes aliasing of out-of-band noise. It also includes the $f_{\text{link}} (\sim 0.7)$ estimated at bath temperature 100 mK. In addition, an offset labeled NEP_γ is calculated from the difference between the simulated low-frequency noise value and the average of the data up to 80 Hz for the 50% R_N dataset. All simulated data are then shifted by this amount. More discussion of NEP_γ can be found below.

The right panel of Fig. 4 shows measured PSD at 20 Hz for most of the HF array for data taken on the telescope. The sample rate for this dataset was 411 Hz. Detectors at the two frequencies were designed to have different values of P_{sat} for optimal function under atmospheric loading, and we therefore expect 230 GHz detectors to have larger NEP if thermal link noise dominates in the dark. The difference observed between the frequencies in the histogram is likely due in part to this, and in part to the higher photon noise in the 230 GHz band.

From this data set, we report the typical value and spread of the on-telescope NEP as $4.0^{+0.7}_{-0.5} \times 10^{-17} \text{ W}/\sqrt{\text{Hz}}$ for 150 GHz detectors, and $6.2^{+0.8}_{-0.7} \times 10^{-17} \text{ W}/\sqrt{\text{Hz}}$ for the 230 GHz detectors. The central value reported is the median of the distributions shown in Fig. 4, where the largest and smallest 2.5% of measured PSD have been cut. The number of detectors cut is ~ 30 for both frequencies. The reported spreads above and below the median are calculated as the difference between the median and the 84th and 16th percentile in the cut distribution, respectively ($\pm 1\sigma$ if normally distributed). The long tail toward values greater than the median will be further studied, especially in relation to achieved noise levels during observation.

To understand our measurements, we need to include the photon noise levels in the telescope contributed by the ambient-temperature window, reflective cover, and (to a much lesser extent) the cold lenses and filters. A naive estimate of the photon noise can be parametrized in terms of the optical power absorbed by the detectors in steady state. Assuming diffraction-limited single-moded throughput for individual detectors, and working

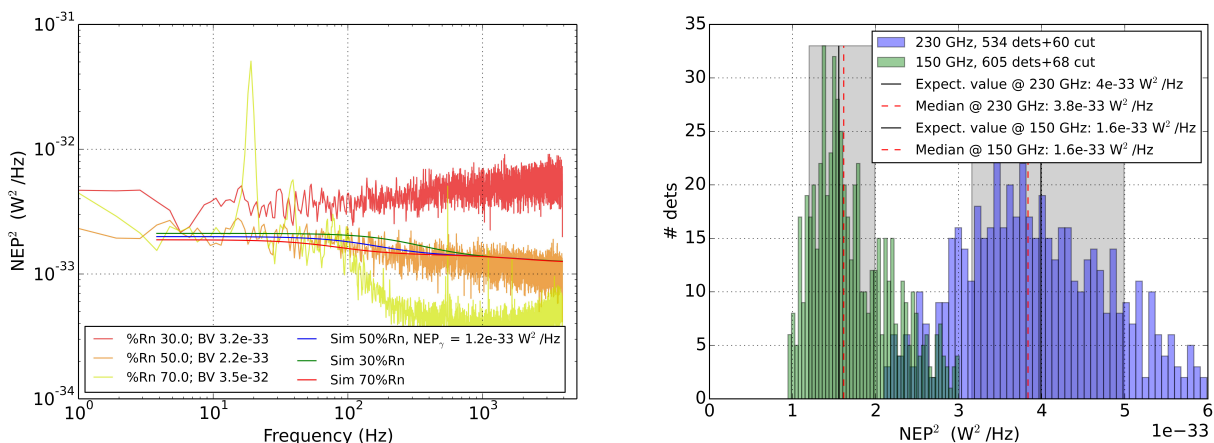


Figure 4: *Left*: Measured PSD data vs. frequency from telescope noise acquisitions at 7.8 kHz sampling rate under different bias conditions. Science observations will take place with detectors biased to 50% R_N and 411 Hz sampling rate. The colored lines represent simulations of the expected detector noise, including aliasing, and a measured offset, likely dominated by photon noise, estimated as the NEP_γ in the legend for this particular device. Values quoted as “BV” in the legends are PSD values averaged in a few bins around 20 Hz. Deviations from the model at 30% and 70% R_N are being investigated. *Right*: Histogram of detector PSD measured at 20 Hz at 120 mK T_{bath} and 60% R_N on the telescope. These data were acquired at a 411 Hz sample rate. Cut detectors are among the top or bottom 2.5%. Typical total PSD values, the sum of NEP_{TL}^2 and NEP_γ^2 , are the solid black lines. Gray bands indicate systematic spread due to systematic effects like transient heating during measurement of saturation powers and miscalibration between telescope and laboratory bath temperatures (see text).

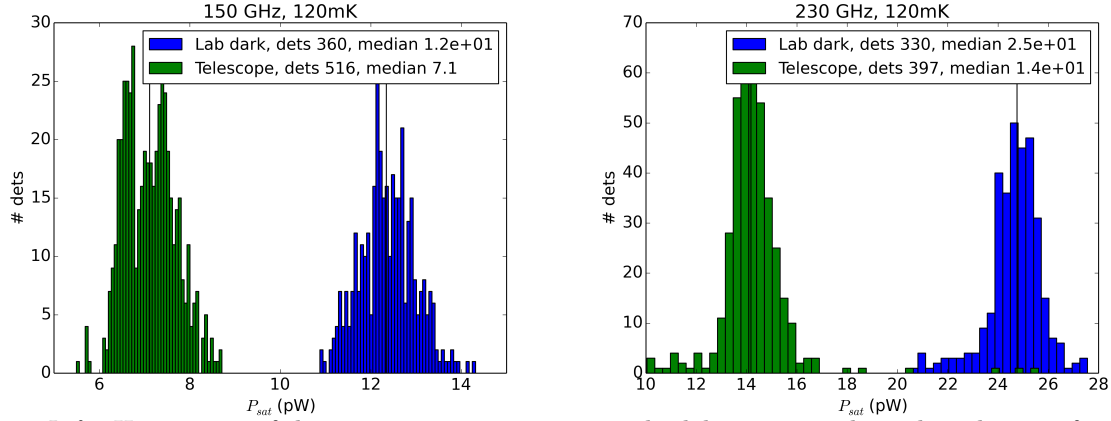


Figure 5: *Left*: Histograms of detector saturation power in the laboratory and on the telescope for 150 GHz detectors at 120 mK bath temperature. *Right*: Identical P_{sat} histograms for 230 GHz detectors. In both, the difference between the medians is used as a rough quantification of optical loading on the telescope.

from equations in Ref. 20, we calculate NEP_{ph}^2 for a single polarization as

$$\text{NEP}_{\gamma}^2 = 2h\nu_o P_{\text{abs}} + \frac{P_{\text{abs}}^2}{\Delta\nu}, \quad (5)$$

with P_{abs} the absorbed optical power on the TES, $\Delta\nu$ the detector bandpass, and ν_o the central frequency in the bandpass.

To estimate P_{abs} , we compare P_{sat} from the laboratory and on the telescope for detectors which were dark in the laboratory. This comparison is done for I-V data taken at the same bath temperature in the two testbeds. Figure 5 shows the results for the 150 and 230 GHz channels in the left and right panels, respectively. A lower bound of 1 pW and an upper bound of 45 pW is applied to the data before plotting and estimating the median, cutting up to ~ 300 detectors per frequency in the laboratory data due to open connections or problems in the readout signal chain. Estimating the loading as 5 and 10 pW for the two channels and bandpasses of 40 and 80 GHz, we calculate $\text{NEP}_{\gamma}^2 = 1.2 \times 10^{-33} \text{ W}^2/\text{Hz}$ for the 150 GHz detectors, and $3.3 \times 10^{-33} \text{ W}^2/\text{Hz}$ for 230 GHz detectors.

The histogram in the right panel of Fig. 4 shows vertical lines indicating our crude estimate of $\text{NEP}_{\text{TL}}^2 + \text{NEP}_{\gamma}^2$. The gray bands indicate the effect of possible systematics, including array heating during the I-V curve acquisition used to calculate P_{sat} , and a possible $\pm 5\text{mK}$ miscalibration of the bath temperatures between the laboratory data and the field. For the detector studied in the left panel of Fig. 4, the measured NEP_{γ} is within the range of photon noise calculated when these effects are taken into account. However, the median NEP_{γ} values appear somewhat high when using these preliminary estimates from telescope data with reflective covers. We will use on-sky data to finalize these measurements.

4. OPTICAL MEASUREMENTS

The optical efficiencies of the detectors are estimated by measuring the radiative power from a blackbody cold load source through a series of low-pass filters and the spline-profiled feedhorns. A gold-coated silicon mask is attached over the feedhorn apertures, covering 2/3 of the pixels and allowing cold load illumination on the other 1/3. The cold load is made of a piece of aluminum plate with square pyramids of height 2 cm and base width 1 cm cut on the surface, which is coated with Eccosorb 110.²¹ The emissivity of the source is measured with a Vector Network Analyzer (VNA) at ambient temperature to be greater than 0.99 within the band of interest. The source is 15 cm by 15 cm wide, and placed 13.5 cm away from the surface of the feedhorn. The source temperature is controlled between 10 and 22 K to avoid overloading the DR mixing chamber plate. Pixels are illuminated through three large-diameter low-pass filters (two of which came from the ACT experiment²²), mounted between the load and the array, on stages at $\sim 100 \text{ mK}$, $\sim 1 \text{ K}$ and $\sim 4 \text{ K}$. These filters have approximate

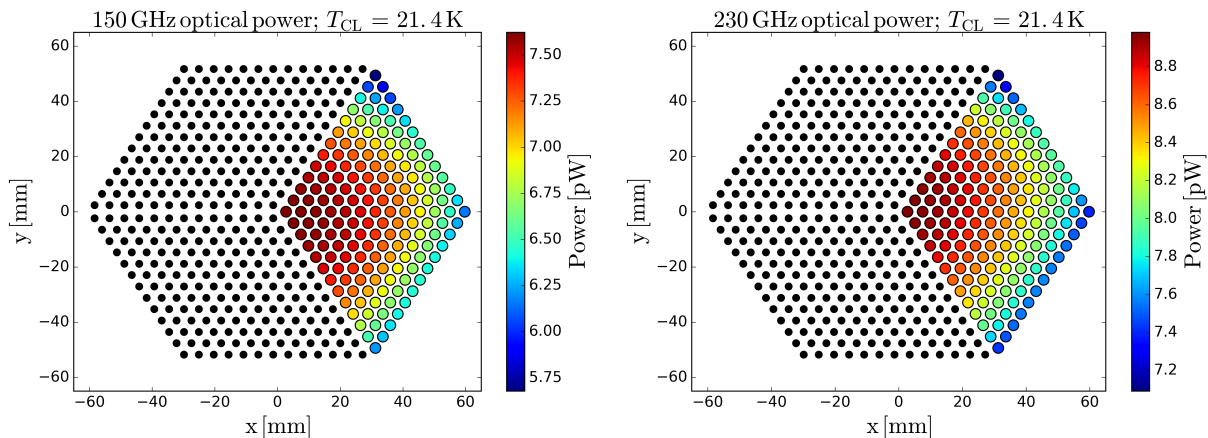


Figure 6: The expected optical power from the direct emission of the blackbody cold load source is computed at each illuminated pixel position for the 150 GHz and 230 GHz frequency bands, considering the beam, cold load solid angle, filter transmission, and the source emissivity (assumed to be unity based on measurements). We use a top-hat response to compute this expected power, with windows between 128 and 170 GHz for the 150 GHz band and 190 and 270 GHz for the 230 GHz band. The power calculated for cold load temperature of 21.4 K is shown as an example. A gold-coated silicon mask is used to illuminate 1/3 of the pixels (shown as colored circles to the right) and cover the rest (shown as black dots). One side of the square-shaped cold load is parallel to the bottom right side of the hexagonal feedhorn, with the center axes aligned. This geometrical asymmetry is seen in the power pattern over the illuminated pixels.

cutoff wave numbers at 11, 12, and 8.5 cm^{-1} respectively. Each low-pass filter is composed of stacks of thin metal-mesh filters, and the transmission spectra have been measured at Cardiff.²³ The beam for the feedhorn is measured with a VNA at ambient temperature and shows good agreement with the model simulated by the High Frequency Structure Simulator (HFSS) software*.²

The detector P_{sat} for both the illuminated and the dark detectors are measured with the bath temperature held at 100 mK and the cold load set to eight temperature values between 11 and 21.4 K. The bath temperature is measured at the copper detector clamp ring, to which the detector wafer is heat sunk through many beryllium copper legs and six gold ribbons.¹¹ Although the thermometer mounted on this ring is held at 100 mK within ± 1 mK as the cold load temperature is varied, P_{sat} for the dark detectors decreases by ~ 1 pW as the cold load temperature increases from 11 to 21.4 K. This is consistent with a slight increase in the actual bath temperature for the detectors.

We assume azimuthal symmetry in the detector wafer to correct for this likely thermal effect when estimating the radiative power on the illuminated detectors. For each illuminated detector, we average the P_{sat} of all dark detectors within a 1 cm width annulus centered at the radius of the given illuminated detector then subtract from it the P_{sat} of the illuminated detector to estimate the optical power, P^{meas} . The average over the dark P_{sat} includes ~ 30 to ~ 250 dark detectors depending on the radius. Changing the annulus width by ± 0.2 cm leads to less than $\sim 0.5\%$ change in the final efficiency estimate. We measure the optical power for all illuminated detectors at each cold load temperature and compare to the calculated optical power to estimate the optical efficiency.

Performing simultaneous optical and dark measurements over a large detector wafer with a large cold load source and three low-pass filters led to a large distance between the feedhorn and the cold load – too large to use a simple beam-filling argument when calculating the optical power, especially for the edge pixels. Hence the solid angle subtended by the square-shaped cold load through the beam pattern is calculated for each pixel position. The HFSS model for the beam pattern is used when performing the solid angle integration at each frequency. For each pixel position and cold load temperature, the total radiative power is calculated considering

*<http://www.ansys.com/Products/Electronics/ANSYS-HFSS>

the beam, cold load solid angle, filter transmission, and the source emissivity with the following expression:

$$P(p, T_{\text{CL}}) = \frac{1}{2} \int \epsilon(\nu) f(\nu) A_e(\nu) P(\nu, \theta, \phi) B(\nu, T_{\text{CL}}) d\Omega d\nu, \quad (6)$$

where p is the pixel position index, T_{CL} is the cold load temperature, $1/2$ is for one polarization, $\epsilon(\nu)$ is the source emissivity (assumed to be unity based on measurements), $f(\nu)$ is the filter transmission, $A_e(\nu)$ is the feedhorn pixel effective area (equal to λ^2/Ω for single-moded operation), $P(\nu, \theta, \phi)$ is the normalized beam pattern, and $B(\nu, T_{\text{CL}})$ is the Planck function. After integrating the angular parts, we are left with

$$P(p, T_{\text{CL}}) = \frac{1}{2} \int f(\nu) \frac{c^2}{\nu^2} \frac{\Omega_{\text{CL}}(p, \nu)}{\Omega_{\text{total}}(\nu)} B(\nu, T_{\text{CL}}) d\nu, \quad (7)$$

where $\Omega_{\text{CL}}(p, \nu)$ is the solid angle subtended by the cold load incorporating the beam pattern at pixel position p , and $\Omega_{\text{total}}(\nu)$ is the total solid angle from integrating the beam pattern. The 8.5 cm^{-1} filter cuts into the high frequency end of the expected passband for the 230 GHz detectors, and this is taken into account with $f(\nu)$ in computing the expected power. We use a top-hat response to calculate the optical power with windows between 128 and 170 GHz for the 150 GHz band and 190 and 270 GHz for the 230 GHz band. The emissive power from the solid angle outside of the cold load is negligible, since it is mostly copper at 1 K through one low-pass filter, or aluminum at 4 K through three low-pass filters. For instance, 4 K radiation with emissivity unity filling the solid angle outside of the cold load for the edge pixels are $<0.2 \text{ pW}$ for the 150 GHz band and less for the 230 GHz band. The calculated optical powers from the cold load for both frequency bands are shown in Fig. 6. Naively assuming beam-filling by the cold load leads to an overestimation of the calculated power, resulting in an underestimation of the optical efficiency by as much as 0.05 to 0.2 for pixels within 20 mm radius, and possibly worse for the outer pixels.

The ratio of the measured power and the calculated power yields the optical efficiency. For each illuminated detector, the measured and calculated powers at all eight cold load temperature steps are simultaneously fitted to the expression

$$P^{\text{meas}}(p, T_{\text{CL}}) = \eta P(p, T_{\text{CL}}) + K, \quad (8)$$

where η is the estimated optical efficiency, K is a constant, $P^{\text{meas}}(p, T_{\text{CL}})$ is the measured optical power, and $P(p, T_{\text{CL}})$ is the calculated optical power (Eq. 7). The estimated optical efficiencies for the two frequency bands are shown as a function of radius in Fig. 7. The mean optical efficiency is ~ 0.65 for the 150 GHz band and ~ 0.55 for the 230 GHz band. The descriptions for lines and bands in the figure are given in the caption. The scatter becomes large as one moves away from the center. Preliminary evidence suggests this increasing spread with radius may be due to differences in coupling between the two polarizations and is being investigated further.

5. CONCLUSION

In this paper, we have reported on progress toward a full characterization of the electrothermal and optical properties of the TES bolometer arrays in Advanced ACTPol. Our results indicate *in situ* detector noise which is consistent with a sum of thermal link and photon noise in the signal band, with a possible excess above $\sim 200 \text{ Hz}$. In a sample device from the array, swept-sine impedance data were successfully used to extract electrothermal parameters and model on-transition noise. The model is consistent with the data up to features in the data which are under investigation. We will investigate measured optical noise levels due to loading to confirm the results in this paper.

We have measured the detector optical efficiencies in laboratory using a cold load blackbody source. Preliminary evidence suggests consistency with the response level seen on the telescope. The source of the scatter in the estimated efficiency is being investigated.

[†]<http://www.sonnetsoftware.com>

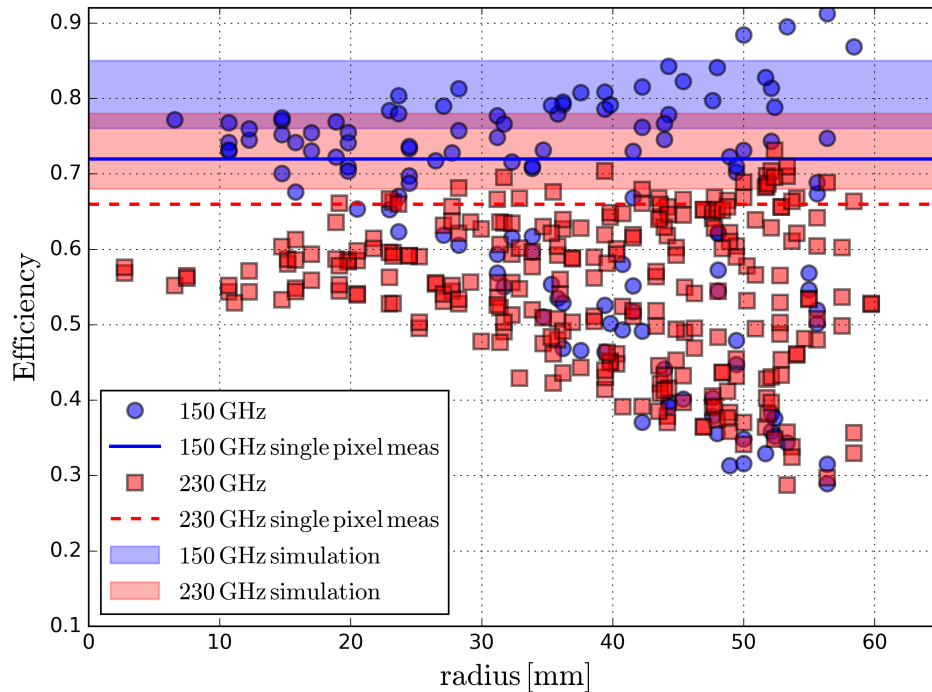


Figure 7: The detector optical efficiency is estimated relative to a top-hat response (frequency windows given in Section 4) and plotted as a function of radius. Blue circles (red squares) show the estimated optical efficiencies for the 150 GHz (230 GHz) detectors. The mean optical efficiency is ~ 0.65 for the 150 GHz band and ~ 0.55 for the 230 GHz band (20% and 10% higher respectively if estimated relative to the measured passbands on prototype single pixel samples). Blue solid line (red dashed line) shows the efficiency measured on prototype 150 GHz (230 GHz) single pixel samples. Wide bands show the range of efficiencies from the uncertainty in the dielectric loss tangent of the silicon nitride lines ($0.0008 < \tan\delta < 0.002$), simulated using Sonnet[†] transmission line modeling of the circuit. Preliminary evidence suggests that the spread in efficiency increasing with radius may be due to differences in coupling between the two polarizations and is being investigated further.

6. ACKNOWLEDGEMENTS

This work was supported by the U.S. National Science Foundation through award AST1440226. The development of multichroic detectors was supported by NASA grants NNX13AE56G. The work of KTC, BJK, and SMS was supported by NASA Space Technology Research Fellowship awards.

REFERENCES

- [1] De Bernardis, F., Stevens, J. R., Hasselfield, M., Alonso, D., Bond, J. R., Calabrese, E., et al., “Survey strategy optimization for the Atacama Cosmology Telescope,” *Proc. SPIE* **9910**, 991014–991014–14 (2016).
- [2] Simon, S. M., Austermann, J., Beall, J. A., Choi, S. K., Coughlin, K. P., et al., “The design and characterization of wideband spline-profiled feedhorns for Advanced ACTPol,” *Proc. SPIE* **9914**, 991416–991416–13 (2016).
- [3] Datta, R., Austermann, J., Beall, J. A., Becker, D., Coughlin, K. P., Duff, S. M., Gallardo, P. A., Grace, E., et al., “Design and deployment of a multichroic polarimeter array on the atacama cosmology telescope,” *Journal of Low Temperature Physics* **184**(3), 568–575 (2016).
- [4] Li, D., Austermann, J. E., Beall, J. A., Becker, D. T., Duff, S. M., et al., “AlMn Transition Edge Sensors for Advanced ACTPol,” *Journal of Low Temperature Physics* **184**(1), 66–73 (2016).

- [5] Duff, S. M., Austermann, J., Beall, J. A., Becker, D., Datta, R., et al., “Advanced ACTPol Multichroic Polarimeter Array Fabrication Process for 150 mm Wafers,” *Journal of Low Temperature Physics* **184**(3), 634–641 (2016).
- [6] Irwin, K. D. and Hilton, G. C., [*Cryogenic Particle Detection*], ch. Transition Edge Sensors, 63–150, Springer Verlag, Berlin (2005).
- [7] Li, Y., Choi, S., Ho, S.-P., Crowley, K. T., Salatino, M., Simon, S. M., Staggs, S. T., et al., “Assembly and integration process of the first high density detector array for the Atacama Cosmology Telescope,” *Proc. SPIE* **9914**, 991435–991435–9 (2016).
- [8] Doriese, W. B., Morgan, K. M., Bennett, D. A., Denison, E. V., Fitzgerald, C. P., Fowler, J. W., et al., “Developments in Time-Division Multiplexing of X-ray Transition-Edge Sensors,” *Journal of Low Temperature Physics* **184**(1), 389–395 (2016).
- [9] Battistelli, E. S., Amiri, M., Burger, B., Halpern, M., Knotek, S., Ellis, M., et al., “Functional Description of Read-out Electronics for Time-Domain Multiplexed Bolometers for Millimeter and Sub-millimeter Astronomy,” *Journal of Low Temperature Physics* **151**(3), 908–14 (2008).
- [10] Henderson, S. W., Stevens, J. R., Amiri, M., Austermann, J., Beall, J. A., Chaudhuri, S., Cho, H.-M., et al., “Readout of two-kilopixel transition-edge sensor arrays for Advanced ACTPol,” *Proc. SPIE* **9914**, 99141G–99141G–17 (2016).
- [11] Ward, J. T., Austermann, J., Beall, J. A., Choi, S. K., Crowley, K. T., Devlin, M. J., et al., “Mechanical design and development of TES bolometer detector arrays for the Advanced ACTPol experiment,” *ArXiv e-prints* (July 2016).
- [12] Thornton, R. J., Ade, P. A. R., Aiola, S., Angile, F. E., Amiri, M., Beall, J. A., Becker, D. T., Cho, H., et al., “The Atacama Cosmology Telescope: The polarization-sensitive ACTPol instrument,” *ArXiv e-prints* (May 2016).
- [13] George, E. M., Austermann, J. E., Beall, J., Becker, D., Benson, B. A., Bleem, L. E., et al., “A Study of Al-Mn Transition Edge Sensor Engineering for Stability,” *Journal of Low Temperature Physics* **176**(3), 383–91 (2014).
- [14] Ho, S. et al., “In preparation,” *Proc. SPIE* **9914** (2016, forthcoming).
- [15] Lindeman, M. A., Barger, K. A., Brandl, D. E., Crowder, S. G., Rocks, L., and McCammon, D., “Complex impedance measurements of calorimeters and bolometers: Correction for stray impedances,” *Review of Scientific Instruments* **78**(4) (2007).
- [16] Zhao, Y., *Characterization of Transition Edge Sensors for the Millimeter Bolometer Array Camera on the Atacama Cosmology Telescope*, PhD thesis, Princeton University (2008).
- [17] Ho, S. P., Pappas, C. G., Austermann, J., Beall, J. A., Becker, D., Choi, S. K., Datta, R., et al., “The First Multichroic Polarimeter Array on the Atacama Cosmology Telescope: Characterization and Performance,” *Journal of Low Temperature Physics* **184**(3), 559–567 (2016).
- [18] Grace, E., *Detector Characterization, Optimization, and Operation for ACTPol*, PhD thesis, Princeton University (2016).
- [19] Mather, J. C., “Bolometer noise: nonequilibrium theory,” *Applied Optics* **21**, 1125–9 (1982).
- [20] Lamarre, J. M., “Photon noise in photometric instruments at far-infrared and submillimeter wavelengths,” *Appl. Opt.* **25**, 870–876 (Mar 1986).
- [21] Fixsen, D. J., Wollack, E. J., Kogut, A., Limon, M., Mirel, P., Singal, J., and Fixsen, S. M., “Compact radiometric microwave calibrator,” *Review of Scientific Instruments* **77**, 064905–064905 (June 2006).
- [22] Swetz, D. S., Ade, P. A. R., Amiri, M., Appel, J. W., Battistelli, E. S., Burger, B., Chervenak, J., et al., “Overview of the Atacama Cosmology Telescope: Receiver, Instrumentation, and Telescope Systems,” *ApJS* **194**, 41 (June 2011).
- [23] Tucker, C. E. and Ade, P. A. R., “Thermal filtering for large aperture cryogenic detector arrays,” *Proc. SPIE* **6275**, 62750T–62750T–9 (2006).